Measurement of iodine species and sulfuric acid using bromide chemical ionization mass spectrometers

Mingyi Wang[1,2*], Xu-Cheng He[3*#], Henning Finkenzeller[4], Siddharth Iyer[3], Dexian Chen[1,5], Jiali Shen[3], Mario Simon[6], Victoria Hofbauer[1,2], Jasper Kirkby[6,7], Joachim Curtius[6], Norbert Maier[8], Theo Kurtén[3,8], Douglas R. Worsnop[3,9], Markku Kulmala[3,10,11,12], Matti Rissanen[3,13], Rainer Volkamer[4], Yee Jun Tham[14,3#], Neil M. Donahue[1,2,5,15], and Mikko Sipilä[3]

[1]Center for Atmospheric Particle Studies, Carnegie Mellon University, Pittsburgh, PA, 15213, USA
[2]Department of Chemistry, Carnegie Mellon University, Pittsburgh, PA, 15213, USA
[3]Institute for Atmospheric and Earth System Research (INAR), University of Helsinki, 00014 Helsinki, Finland
[4]Department of Chemistry & CIRES, University of Colorado Boulder, Boulder, CO 80309, USA
[5]Department of Chemical Engineering, Carnegie Mellon University, Pittsburgh, PA, 15213, USA
[6]Institute for Atmospheric and Environmental Sciences, Goethe University Frankfurt, 60438 Frankfurt am Main, Germany
[7]CERN, the European Organization for Nuclear Research, CH-1211 Geneve 23, Switzerland
[8]Department of Chemistry, University of Helsinki, 00014 Helsinki, Finland
[9]Aerodyne Research, Inc., Billerica, MA, 01821, USA
[10]Helsinki Institute of Physics, P.O. Box 64 (Gustaf Hallstromin katu 2), FI-00014 University of Helsinki, Finland
[11]Joint International Research Laboratory of Atmospheric and Earth System Sciences, Nanjing University, Nanjing, China
[12]Aerosol and Haze Laboratory, Beijing Advanced Innovation Center for Soft Matter Science and Engineering, Beijing University of Chemical Technology, Beijing, China
[13]Aerosol Physics Laboratory, Physics Unit, Faculty of Engineering and Natural Sciences, Tampere University, Tampere, Finland
[14]School of Marine Sciences, Sun Yat-sen University, Zhuhai 519082, China
[15]Department of Engineering and Public Policy, Carnegie Mellon University, Pittsburgh, PA, 15213, USA
[*]These authors contributed equally to this work

[#]*Correspondence to*:
Xu-Cheng He (xucheng.he@helsinki.fi) and Yee Jun Tham (thamyj@mail.sysu.edu.cn).

Abstract. Iodine species are important in the marine atmosphere for oxidation and new-particle formation. Understanding iodine chemistry and iodine new-particle formation requires high time resolution, high sensitivity, and simultaneous measurements of many iodine species. Here, we describe the application of bromide chemical ionization mass spectrometers (Br-CIMS) to this task. During the iodine oxidation experiments in the Cosmics Leaving OUtdoor Droplets (CLOUD) chamber, we have measured gas-phase iodine species and sulfuric acid using two Br-CIMS, one coupled to a Multi-scheme chemical IONization inlet (Br-MION-CIMS) and the other to a Filter Inlet for Gasses and AEROsols inlet (Br-FIGAERO-CIMS). From offline calibrations and inter-comparisons with other instruments, we have quantified the sensitivities of the Br-MION-CIMS to HOI, I_2, and H_2SO_4 and obtain detection limits of 5.8×10^6, 3.8×10^5, and 2.0×10^5 molec cm^{-3}, respectively, for a 2-min integration time. From binding energy calculations, we estimate the detection limit for HIO_3 to be 1.2×10^5 molec cm^{-3}, based on an assumption of maximum sensitivity. Detection limits in the Br-FIGAERO-CIMS are around one order of magnitude higher than those in the Br-MION-CIMS; for example, the detection limits for HOI and HIO_3 are 3.3×10^7 and 5.1×10^6 molec cm^{-3}, respectively. Our comparisons of the performance of the MION inlet and the FIGAERO inlet show that bromide chemical ionization

46 mass spectrometers using either atmospheric pressure or reduced pressure interfaces are well-matched to measuring

47 iodine species and sulfuric acid in marine environments.

48

49 **1 Introduction**

50 Reactive iodine species are released into the atmosphere mainly by biological processes in marine environments (i.e.

51 from macro- and micro-algae) (McFiggans et al., 2004), O_3 deposition on the sea surface (Carpenter et al., 2013), as

52 well as from the sea ice (Spolaor et al., 2013) and snowpack in the polar region (Raso et al., 2017). Once emitted,

53 iodine species can modify atmospheric oxidative capacity via a chain of catalytic reactions with O_3 that form iodine

54 oxides, leading to about 20–28 % of O_3 loss in the marine boundary layer (Prados-Roman et al., 2015; Sherwen et al.,

55 2016). Through convection, reactive iodine species can be transported from the lower troposphere to the upper

56 troposphere-lower stratosphere, causing one third of the iodine-induced ozone loss in the upper troposphere-lower

57 stratosphere (Koenig et al., 2020). Another important effect of iodine species is their contribution to atmospheric new-

58 particle formation. O'Dowd et al. (O'Dowd et al., 2002) showed that particles are produced from condensable iodine-

59 containing vapors at a costal location (Mace Head in Ireland). Recent studies have demonstrated that iodine oxoacids

60 (iodous acid, HIO_2 and iodic acid, HIO_3) dominate the iodine cluster formation processes (He et al., 2021a, 2021b),

61 and drive the bursts of freshly-formed particles in coastal regions (Sipilä et al., 2016). This process thereby may

62 enhance cloud condensation nuclei formation, affecting climate both directly and indirectly (Saiz-Lopez et al., 2012;

63 Simpson et al., 2015).

64

65 Understanding iodine chemistry and iodine driven new-particle formation requires high time resolution, high

66 sensitivity, and simultaneous measurements of iodine species. However, this has been a long-standing challenge due

67 to their low abundance and short atmospheric lifetimes. Previous studies have achieved detection of relatively more

68 abundant molecular iodine (I_2), iodine monoxide (IO), and iodine dioxide (OIO) via optical spectroscopy, such as

69 differential optical absorption (Leigh et al., 2010), cavity ring-down (Bitter et al., 2005), cavity enhanced absorption

70 (Vaughan et al., 2008), laser-induced fluorescence (Dillon et al., 2006), and resonance fluorescence (Gómez Martín

71 et al., 2011). The spectroscopic techniques are invaluable; however, their very specificity limits them to the detection

72 of a few iodine compounds, and they are less sensitive to other iodine species that have congested or broad absorption

73 features, such as hypoiodous acid (HOI) and iodic acid (HIO_3).

74

75 Another commonly used technique is mass spectrometry; it has a fast response time and a low detection limit, but

76 extra calibration efforts are needed for the quantification of the detection sensitivity. For example, photoionization

77 (Gómez Martín et al., 2013) and chemical ionization mass spectrometry (CIMS) have been employed to detect a suite

78 of halogen species. Reagent ions used with CIMS include: SF_5^- for HCl and $ClONO_2$ (Marcy et al., 2004); iodide (I^-)

79 for atmospheric chlorine and bromine species such as $ClNO_2$, Cl_2, ClO, BrO, and BrCl (Kercher et al., 2009; Lee et

80 al., 2018; Tham et al., 2016); superoxide (O_2^-) for molecular iodine (I_2) (Finley and Saltzman, 2008); and both nitrate

81 (NO_3^-) (Sipilä et al., 2016) and protonated water (H_3O^+) (Pfeifer et al., 2020) for HIO_3. The nitrate-CIMS and H_3O^+-

82 CIMS suffer from the limited analyte affinity to the reagent ions. The iodide-CIMS can effectively measure chlorine

83 and bromine species, but it is not suitable to detect iodine species due to the ambiguity in peak identification.

84

85 The bromide ion (Br^-) exhibits an affinity to a wide spectrum of iodine containing species. Br-CIMS has been routinely

86 used to measure chlorine species (Lawler et al., 2011), HO_2 radicals (Sanchez et al., 2016), organic vapors and sulfuric

87 acid (Rissanen et al., 2019), and nitric acid (Wang et al., 2020). Like chlorine species, iodine species are known to

88 cluster with bromide ions via halogen (or hydrogen) bonds; as such, here we explore using the Br-CIMS to measure

89 gas-phase iodine species and sulfuric acid simultaneously at concentrations relevant to the marine boundary layer. In

90 this study, we demonstrate the detection of various gas-phase inorganic iodine species with the Br-CIMS and explore

91 the effect of relative humidity (RH) on that detection. We then quantify the sensitivities of several gas-phase iodine

92 species via inter-method calibration, offline calibration, and quantum chemical calculations. Finally, we compare the

93 performance of Br-MION-CIMS and Br-FIGAERO-CIMS and show that both of them are well-suited for iodine

94 species measurement in the marine boundary layer.

95

96 **2 Methodology**

97 **2.1 The CLOUD facility**

98 We conducted measurements and instrument inter-comparison at the CERN CLOUD facility, a 26.1 m^3

99 electropolished stainless-steel chamber that enables new-particle formation experiments simulating the typical range

100 of tropospheric conditions with scrupulous cleanliness and minimal contamination (Duplissy et al., 2016; Kirkby et

101 al., 2011). The CLOUD chamber is mounted in a thermal housing, capable of keeping temperature constant in a range

102 of -65 ℃ and +100 ℃ with ±0.1 ℃ precision (Dias et al., 2017) and relative humidity commonly between < 0.5 %

103 and 80 %. Photochemical processes are driven by different light sources, including four 200 W Hamamatsu Hg-Xe

104 lamps with significant spectral irradiance between 250 and 450 nm, and an array of 48 green light LEDs at 528 nm

105 with adjustable optical power up to 153 W. Ion-induced nucleation under different ionization levels is simulated with

106 a combination of electric fields (electrodes at ±30 kV at top and bottom of the chamber) which can be turned on to

107 rapidly scavenge smaller ions, and a high-flux beam of 3.6 GeV pions (π^+) which enhances ion production when turned

108 on. Mixing is accelerated with magnetically coupled fans mounted at the top and bottom of the chamber. The

109 characteristic gas mixing time in the chamber during experiments is a few minutes. The loss rate of condensable vapors

110 onto the chamber wall is comparable to the condensation sink in pristine boundary layer environments (e.g. 2.2×10^{-3}

111 s^{-1} for H_2SO_4 at 5 ℃). To avoid a memory effect between different experiments, the chamber is periodically cleaned

112 by rinsing the walls with ultra-pure water and heating to 100 ℃ for at least 24 hours, ensuring extremely low

113 contaminant levels of sulfuric acid ($< 5 \times 10^4$ cm^{-3}) and total organics (< 150 pptv) (Kirkby et al., 2016; Schnitzhofer

114 et al., 2014). The CLOUD gas system is also built to the highest technical standards of cleanliness and performance.

115

116 The dry air supply for the chamber is provided by cryogenic nitrogen (Messer, 99.999 %) and cryogenic oxygen

117 (Messer, 99.999 %) mixed at the atmospheric ratio of 79:21. Ultrapure water vapor, ozone and other trace gases can

118 be precisely added to attain desired mixing ratios at different levels. The total injection rate of the humidified air is

119 fixed at 330 standard liters per minute (slpm) to compensate for the sampling consumption of various instruments.

120 Molecular iodine (I_2) is injected into the chamber by passing a flow of cryogenic nitrogen through a crystalline iodine

121 (I_2, Sigma-Aldrich, 99.999 % purity) reservoir, which is temperature-controlled at 10 ℃, to achieve levels of 0.4 to

122 168 pptv in the chamber. The sulfinert-coated injection lines are temperature stabilized to minimize line conditioning

123 effects. High intensity green light emitting diodes (LEDs) are used to photolyze molecular iodine into iodine atoms

124 and initiate the subsequent oxidation reactions in the presence of ozone and water vapor. The 48 green LEDs (light

125 sabre 4, LS4) are mounted in pairs (one upward facing, one downward facing) on a copper cooling bar within a long

126 quartz jacket that protrudes into the chamber in the mid plane. The maximum total optical power output is 153 W,

127 centered on 528 nm. Actinic fluxes are regulated by controlling the number of LEDs used and the set point of

128 individual LEDs. Light fluxes are monitored by two photodiodes and a spectrometer.

129

130 **2.2 Br-MION-CIMS**

131 We measured gas-phase iodine species with a bromide chemical ionization atmospheric pressure interface time-of-

132 flight mass spectrometer (Junninen et al., 2010) coupled with a Multi-scheme chemical IONization inlet (Br-MION-

133 CIMS) (Rissanen et al., 2019). The Br-MION inlet consists of an electrically grounded 24 mm inner diameter stainless

134 steel flow tube, attached to an ion source. For the CLOUD measurements, the length of the sampling inlet was ~1.5

135 m and was designed to be in a laminar flow with a fixed total flow rate of 32 standard liters per minute (slpm). An ion

136 filter, operated with positive and negative voltage, was placed at the front of the inlet to filter out any ions in the

137 sample air prior to ion-molecule reaction chamber in the inlet. The reagent ions, bromide (Br^-) and the bromide-water

138 cluster ($H_2O\cdot Br^-$), were produced by feeding 25 standard milliliters per minute (mlpm) of nitrogen (N_2) flow through

139 a saturator containing dibromomethane (CH_2Br_2; > 99.0 %, Tokyo Chemical Industry) into the ion source, where the

140 reagent was ionized by soft X-ray radiation. The resulting ions were then accelerated by a 2800 V ion accelerator array

141 and focused by a 290 V ion deflector into the laminar sampling flow of the inlet via a 5 mm orifice. A small counter

142 flow (~40 mlpm) was applied through the orifice to prevent any mixing of the electrically neutral reagent vapor with

143 the sampling flow. The details of the inlet design, setup, and operation are described previously (He, 2017; Rissanen

144 et al., 2019).

145

146 **2.3 Br-FIGAERO-CIMS**

147 We also measured both the gas- and particle-phase compositions via thermal desorption using a bromide chemical

148 ionization time-of-flight mass spectrometer equipped with a Filter Inlet for Gases and AEROsols (Br-FIGAERO-

149 CIMS) (Lopez-Hilfiker et al., 2014). FIGAERO is a manifold inlet for a CIMS with two operating modes. In the

150 sampling mode, gases are directly sampled into a 150 mbar ion-molecule reactor, using coaxial core sampling to

151 minimize their wall losses in the sampling line. The total flow is maintained at 18.0 slpm and the core flow at 4.5 slpm;

152 the CIMS samples at the center of the core flow with a flow rate at ~1.6 slpm. Concurrently, particles are collected on

153 a PTFE filter via a separate dedicated port with a flow rate of 6 slpm. In the desorption mode, the filter is automatically

154 moved into a pure N_2 gas stream flowing into the ion molecule reactor, while the N_2 is progressively heated upstream

155   of the filter to evaporate the particles via temperature programmed desorption. Analytes are then chemically ionized

156   by Br^- and extracted into a mass spectrometer.

157

158   We optimize the adduct-ion signals in both the Br-MION-CIMS and Br-FIGAERO-CIMS by tuning the electric field

159   strengths in the first two low-pressure stages of the mass spectrometer as weak as possible to minimize collision

160   induced cluster fragmentation while maintaining sufficient ion transmission. Optimization is achieved by maximizing

161   the ratio of I_2Br^-/Br^- at a constant I_2 concentration. We list relevant instrument specifications and operational

162   conditions in Table S1. It should be noted that these values are specific to our instruments, thus can vary according to

163   instrument parameters and may not be applicable to other instruments.

164

165   **2.4 CE-DOAS**

166   For the quantitative measurement of gas-phase molecular iodine (I_2), we deployed a Cavity Enhanced Differential

167   Optical Absorption Spectroscopy instrument (CE-DOAS) (Meinen et al., 2010). CE-DOAS determines concentrations

168   of trace gases from the strength of differential spectral features in a reference spectrum. The overall accuracy for the

169   I_2 time series is estimated to be 20 %, never better than the detection limit (3-sigma precision), resulting from the

170   uncertainty in cross sections and the stability of the baseline. It is thus an absolute method and does not depend on an

171   instrument specific detection efficiency. To maximize the measurement sensitivity towards I_2, we used a setup

172   optimized for the green wavelength range (508-554 nm), where I_2 exhibits strong differential absorption features. The

173   measurement light is provided by a green light emitting diode (LED Engin). Spectral dispersion is established with a

174   Czerny-Turner grating spectrometer (Princeton Instruments Acton 150), resulting in an optical resolution of 0.73 nm

175   full width at half maximum at 546 nm. Intensities are monitored with a CCD detector (Princeton Instruments

176   PIXIS400B) cooled to -70 ℃. Highly reflective mirrors (Advanced Thin Films) enhance the 1 m mirror separation to

177   an effective optical path length of 15-23 km. The effective spectral mirror reflectivity was established by comparing

178   light intensity spectra in the presence of N_2 and He (Washenfelder et al., 2008). The abundance of trace gases is then

179   determined by comparing spectra of chamber air relative to reference spectra recorded with ultrapure N_2 without I_2.

180   Chamber air is drawn into the cavity with a constant flow rate of 1 slpm. Variations of the sampling flow did not result

181   in changes in measured I_2 concentrations, indicating that photolysis from the measurement light within the instrument

182   was negligible. The following absorbers were included in the fit: I_2 (Spietz et al., 2006), NO_2 (Vandaele et al., 1998),

183   H_2O (Rothman et al., 2010), O_2-O_2 collision-induced absorption (Thalman and Volkamer, 2013), and a polynomial of

184   sixth order. The setup allowed a 1-minute detection limit of 25 pptv, or 8 pptv for integration times of 10 minutes,

185   respectively. Periodic automated recordings of N_2 reference spectra were recorded to ensure baseline stability. The

186   optical path length at the time of measurement was continuously confirmed for consistency by the measurement of

187   the O_2-O_2 collision-induced absorption and H_2O column in the same analysis window. The overall systematic accuracy

188   for the I_2 time series is estimated to be 20 %, never better than the detection limit, resulting from the uncertainty in

189   cross sections and the stability of the baseline.

190

191   **2.5 Offline calibration setup**

2.5.1 I_2 permeation device

We used an iodine permeation tube (VICI Metronic) as a source for offline laboratory calibration. The permeation tube was encased within an electronically controlled heating mantle (80 ~ 140 (± 2) ℃) to allow for adjustable yet steady iodine permeation rates. The heating device (for holding the permeation tube) was made from a stainless steel tube (½-inch outer diameter, OD) with a length of 25 cm, encased within an electronically controlled heating mantle. The configuration of the permeation device has been described in Tham et al. (Tham et al., 2021). The iodine permeation device was run continuously for at least 72 hours before any calibration experiments to ensure that a complete equilibrium was reached in the system. We then confirmed the robustness of the permeation device by the constant I_2 signal measured with Br-MION-CIMS for over 24 hours.

To determine the permeation rate of I_2, we trapped iodine in n-hexane at cryogenic temperatures in an all-glass apparatus, following the method described in Chance et al. (Chance et al., 2010). We initially filled the absorption glass vessel with 20 ml n-hexane (99.95 %, Merck), and then weighed it to determine the combined mass. We then immersed the absorption vessel into a wide-necked Dewar vessel, filled with an acetone/dry ice mixture (at -80 ± 3 ℃). After temperature equilibration, the I_2 molecules, carried by 50 mlpm N_2 flow from the permeation device, were bubbled through the absorption vessel. After a continuous collection for 5 hours, we removed the absorption apparatus from the cooling mixture, and allowed it to warm to room temperature prior to disassembling the setup to prevent any losses of iodine on the tip of the inlet capillary. The absorption vessel was then re-weighed; the mass compared with that prior to absorption was less than 2 %, indicating a negligible loss during the trapping process. The I_2 / n-hexane sample solutions were stored at 4 ℃ for 14 hours before being subjected to analysis.

We determined the I_2 concentration of the samples using a UV/Vis spectrophotometer (Shimadzu Model UV2450) at a wavelength of 522 nm. We established a calibration curve via a set of I_2 solutions ranging from 270 to 5300 nmol, diluted with n-hexane from a freshly prepared stock solution (0.5 g L^{-1}). Repetition of the same analysis after 2 and 7 days yielded identical results, confirming that the sample solutions were stable at 4 ℃. As an alternative analytical approach, we also quantified the I_2 concentration in the sample solutions using an inductively coupled plasma mass spectrometer (ICP-MS, Agilent 7800). Before introducing to the ICP-MS, the sample solutions were treated with $NaHSO_3$ water solution (0.100 M), accomplishing efficient hexane-to-water extraction and simultaneous reduction of iodine to iodide (Schwehr et al., 2005) (Agilent Clinical Sample Preparation Guide (v3), *ref.* ISO 17294-2). The ICP-MS results were in good agreement (within 20 % discrepancies) with those from the UV/Vis spectrophotometry.

We conducted the I_2 trapping and quantification experiments in triplicate with satisfactory reproducibility (standard deviation < 10 %). The calculated iodine permeation rate at 50 mlpm N_2 flow and 140 ℃ oven temperature is 278 $\pm$ 12 ng min^{-1} (mean $\pm$ standard deviation). This result was used as the benchmark to estimate temperature-corrected permeation rates according to the formula provided by the permeation tube vendor (VICI Metronic). We checked the validity of the temperature-corrected values by conducting a second iodine absorption experiment in which the iodine

228   permeation tube was kept at 130 ℃ with an N_2 flow rate of 50 mlpm, and the determined permeation rate agreed

229   within 10 % of the calculated value.

230

231   **2.5.2 Cl_2 permeation device**

232   We used a commercial chlorine permeation tube (VICI Metronic) as a source for offline calibration. We passed a 20

233   mlpm high-purity nitrogen (99.999 %) flow at room temperature through a 25 cm long stainless-steel tube (½" O.D.)

234   containing the permeation tube. We quantified the permeation rate of Cl_2 following a procedure described in a previous

235   study (Finley and Saltzman, 2008). The output of 20 mlpm flow was bubbled into a buffered aqueous potassium iodide

236   solution (2.0 % KI (*m/v*), prepared in 1.00 mM aqueous phosphate buffer, pH = 7.0) filled in an all-glass two-stage

237   serial absorption apparatus (stage 1 = 100 ml; stage 2 = 50 ml) for 3 hours and kept at room temperature. The Cl_2

238   oxidized the iodide (I^-) into iodine (I_2) once contacting with the KI absorption solution, and the I_2 further reacted with

239   the excess KI present in the absorption solution to form I_3^-, which can be quantified by UV/Vis-spectrophotometry.

240   We analyzed the resulting sample solutions with an UV/Vis spectrophotometer (Shimadzu Model UV-1800) using 1-

241   cm quartz cells at 352 nm, corresponding to the I_3^-. We detected no I_3^- in the second stage absorption solution,

242   indicating that all the chlorine was quantitatively trapped and rapidly converted to I_3^- within the first absorption unit.

243   The samples were quantified relative to I_3^- standards in the range of 5 to 68×10^{-6} M, prepared by dilution of a stock

244   obtained by dissolving 174 mg iodine in 200 ml of a solution containing 2 % KI in 1.00 mM aqueous phosphate buffer,

245   pH 7.0. From this calibration curve, we calculated a molar absorptivity of 26,800 L mol^{-1} cm^{-1}, which is consistent

246   with the values reported in the literature (Finley and Saltzman, 2008; Kazantseva et al., 2002). Samples and standard

247   solutions were re-analyzed after being stored in the dark at room temperature for 24 hours, and the results were within

248   3 % of those obtained with the fresh solutions. We repeated the absorption experiment, and the calculated chlorine

249   permeation rate at room temperature was 764 ± 74 ng Cl_2 min^{-1} (mean $\pm$ standard deviation).

250

251   **2.5.3 HOI calibrator**

252   We produced a continuous HOI source via the reaction of I_2 and hydroxyl radicals (OH) in a setup similar to the

253   sulfuric acid (H_2SO_4) calibrator (Kürten et al., 2012). The OH was generated by photolyzing H_2O with a mercury (Hg)

254   lamp at 184.9 nm, whose calibrated intensity was used to estimate the OH concentration. We tested the system by

255   removing the I_2 or OH source from the calibrator, upon which HOI production was undetectable, confirming that any

256   single reactant did not produce HOI. A numerical model was constructed to predict the mean HOI concentration

257   entering the Br-MION-CIMS, which is analogous to the model used for H_2SO_4 calibration (Kürten et al., 2012). We

258   only included the formation pathway of I_2 + OH to HOI in the model for simplicity; the other pathway of IO + HO_2

259   was considered minor as its reaction rate is about an order of magnitude slower than that of I_2 + OH. Furthermore, IO

260   is likely at negligible concentration in the calibration device due to the absence of O_3 for IO formation.

261

262   **2.6 Quantum chemical calculations**

263   We used quantum chemical calculations to estimate the cluster formation enthalpy of halogen containing species and

264   bromide ions. The initial conformational sampling was performed using the Spartan '14 program. The cluster

265	geometry was then optimized using density function theory methods at the ωB97X-D/aug-cc-pVTZ-PP level of theory
266	(Chai and Head-Gordon, 2008; Kendall et al., 1992). Iodine pseudopotential definitions were taken from the EMSL
267	basis set library (Feller, 1996). Calculations were carried out using the Gaussian 09 program (Frisch et al., 2010). An
268	additional coupled-cluster single-point energy correction was carried out on the lowest energy geometry to calculate
269	the final cluster formation enthalpy. The coupled-cluster calculation was performed at the DLPNO-CCSD(T)/def2-
270	QZVPP level using the ORCA program ver. 4.0.0.2 (Neese, 2012; Riplinger and Neese, 2013). In Table 1 we present
271	calculated cluster formation enthalpies based on the optimized geometries.

3 Results and Discussion

3.1 Detection of gas-phase inorganic species by Br-MION-CIMS

We show in Fig. 1 the selected inorganic species observed with the Br-MION-CIMS during an iodine oxidation experiment in the CLOUD chamber. The peak identities are indicated in the labels. Observed species include I_2 and its various oxidation products. There are also a few other halogen-containing inorganic species such as Cl_2, ICl and IBr, likely coming from the impurities in the iodine source. Non-halogen inorganic species such as H_2SO_4 can also react with bromide ions and are detected. Due to the large negative mass defect of the bromine and iodine atoms, and the high resolution (~10000 Th Th^{-1}) of the mass spectrometer, the peaks can be unambiguously distinguished and identified in the mass spectrum. As shown in the lower panel of Fig. 1, most of the iodine-containing species appear as a single peak in the unit mass range, except for HIO_2 $^{79}Br^-$ (m/z = 238.82), which overlaps with the reagent ion cluster $(^{79}Br_2^{81}Br)^-$ (m/z = 238.75).

The iodine oxidation experiments were conducted under experimental conditions typically found in the high-latitude marine boundary layer, with a temperature of -10 °C and a relative humidity of 69 %. As illustrated in Fig. 2, a typical experiment started with illumination of the chamber at constant I_2 (~60 pptv) using the green light to photolytically produce I atoms. The subsequent reactions of I and ~ 40 ppbv O_3 led to the formation of various oxidized iodine species within a few minutes. The most prominent species we observed from these experiments were IO, HOI and HIO_3, with lower but significant levels of OIO, HIO_2, and I_2O_4. Among these iodine oxides, IO rose the most rapidly; this is consistent with the first-generation production of IO from the I + O_3 reaction. After a few steps of radical reactions, OIO, HIO_2 and HIO_3 reached steady state almost simultaneously. The only observed iodine oxide dimer was I_2O_4 in this event, while I_2O_2, I_2O_3 and I_2O_5 were below the detection limit of both mass spectrometers. A noticeable dip in the HIO_3 traces a few minutes after the onset of the reactions is likely due to the participation of HIO_3 in new-particle formation, resulting in an extra loss term and a lower steady-state concentration. When we turned off the green light, the production of I radicals stopped and iodine species decayed away.
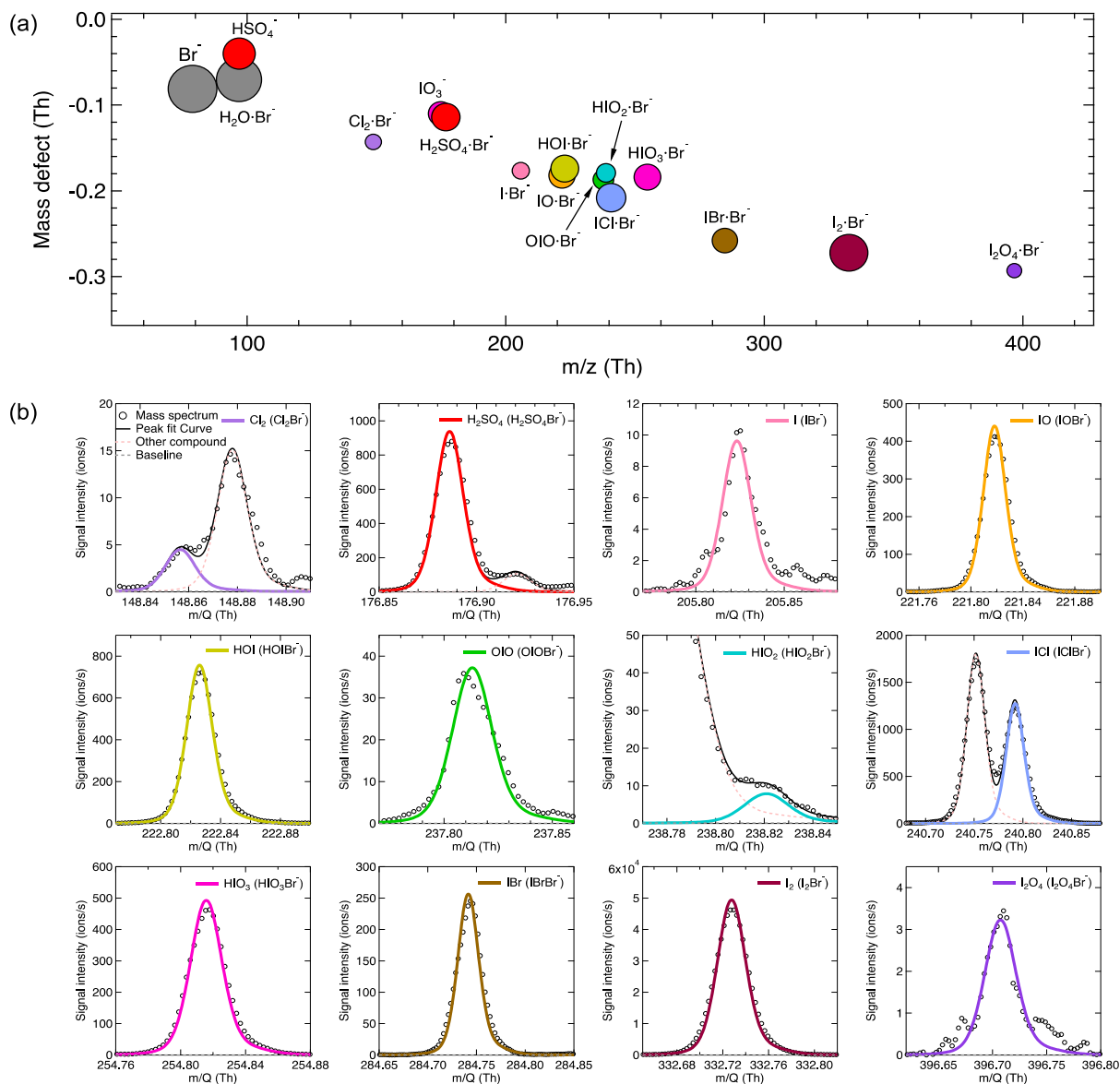
297
298 **Figure 1**. Gas-phase inorganic species measured with the Br-MION-CIMS. (a) Mass defect (difference of exact mass to integer
299 mass) versus m/z of gas-phase halogen species and sulfuric acid during an iodine oxidation experiment at 69 % relative humidity
300 and -10 ℃ (conducted on 05 October 2018). Ions shown here are either clustered with or formed via proton transfer to a bromide
301 ion. The area of the markers is proportional to the logarithm of the signal (counts per second). (b) The high-resolution single peak
302 fits for species in the mass defect plot in the upper panel. Species in both panels are color-coded in the same style.
303
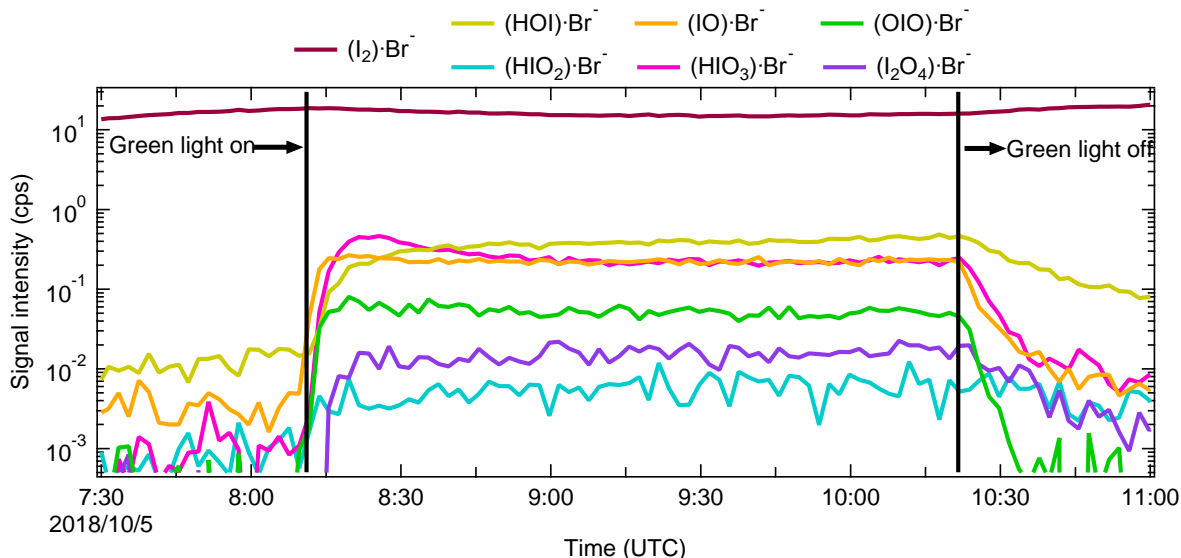
304
305 **Figure 2**. Evolution of selected iodine species during a typical run. The experiment was performed at 60 pptv I_2, 40 ppbv O_3, 69 %
306 relative humidity and -10 °C. The oxidized iodine species start to appear soon after switching on the green light at 08:11, 05 October
307 2018. The I atom production was halted at 10:21, 05 October 2018 by switching off the green light, and the concentration of
308 oxidized iodine species decayed away afterwards. All species are color-coded in the same way as in Fig. 1.
309

310 **3.2 Relative humidity dependence**

311 Water molecules can cluster with I^- to form $H_2O \cdot I^-$ in the iodide CIMS. This enhances the instrument sensitivities for

312 small molecules (i.e. chlorine and bromine) and reduces them for large molecules (i.e. oxygenated organics) (Lee et

313 al., 2014). To investigate the role of water concentration in the sensitivity of the Br-MION-CIMS, we varied the

314 relative humidity (RH) from 40 % to 80 % at a constant temperature of -10 °C. We show in Fig. 3 the correlation of

315 I_2 time series from the Br-MION-CIMS and the CE-DOAS throughout the experiment.

316

317 Chemical ionization relies on an ion-molecule reaction to transfer charge from a reagent ion to an analyte, forming

318 either a product ion or a charged cluster between the analyte and the reagent ion with a rate coefficient k_{IM}. This occurs

319 in an ion-molecule reactor, with a fixed flow rate and thus reaction time, dt, and ideally under pseudo first-order

320 conditions where a small fraction of the analyte is ionized and the reagent ion concentration ([Ion]) remains constant.

321 Under these (linear) conditions the fraction of analyte that is ionized is $k_{IM} \times$ [Ion] $\times dt$. However, the primary ion

322 source strength can vary with time, and so we normalize the analyte signal by reagent ion signal to account for those

323 small variations in analyte signal.

324

325 During the RH transition, the ratio of the two reagent ions, Br^- and $H_2O \cdot Br^-$, changed in the Br-MION-CIMS. As

326 shown in Fig. 3 (a) and (b), using either reagent ion alone for I_2 normalization results in discrepancies in recovered I_2

327 concentrations at different RH. However, if we use the sum of these two reagent ions ($Br^- + H_2O \cdot Br^-$) for normalization,

328 the humidity effect vanishes, as shown in Fig. 3 (c). Separately, during the I_2 calibration using a permeation tube

329 (section 3.3.2.1), the detection of I_2 molecules is robust and independent of RH between 20 % and 40 % at 25 °C, as

330 long as a proper normalization method is used for the Br-MION-CIMS. Furthermore, we have also carried out the

331 HOI calibration at 25 °C (section 3.3.2.3) and used the same normalization method. During the calibration, we varied

332 the water content in the calibrator to vary OH concentrations. A good correlation between the modeled HOI
333 concentrations and the measured HOI signals also indicates that the different H_2O concentrations in the system do not
334 affect the HOI detection (Fig.4(d)). This assertion may also be applicable to molecules such as iodine monochloride
335 (ICl) and iodine monobromide (IBr), which share similar chemical and physical properties with I_2; however, further
336 confirmation is needed for other species such as oxygenated organics.

337
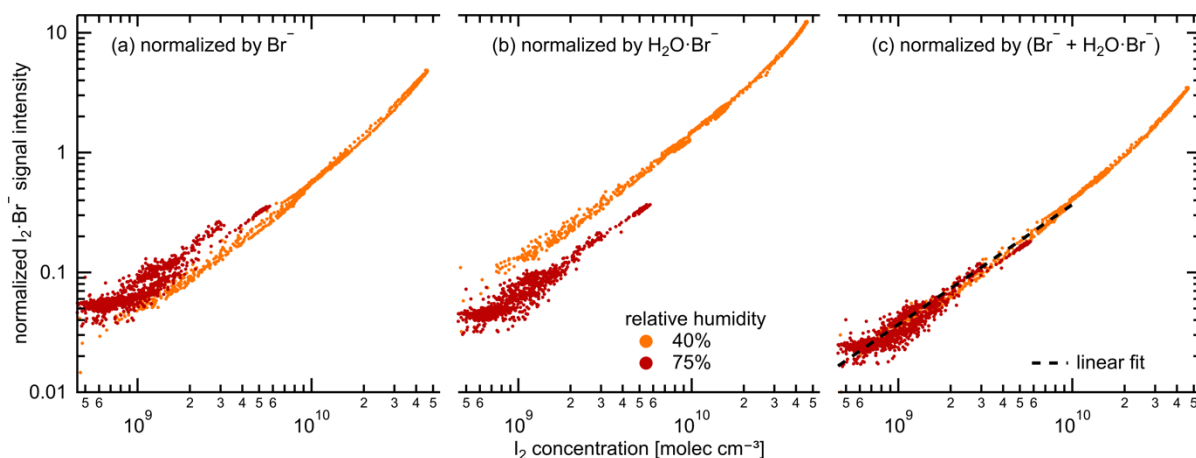
Figure 3. Signal normalization methods for the Br-MION-CIMS. Normalized $I_2 \cdot Br^-$ signal intensity for variable I_2 concentrations, color coded by relative humidity (orange: 35-45 % relative humidity, red: 70-80 % relative humidity). The charger ions in the ion source of Br-MION-CIMS are Br^- and $H_2O \cdot Br^-$ (both ^{79}Br and ^{81}Br). Their abundance depends both on the instrument tuning and the absolute humidity of the sampled flow. The normalization of the $I_2 \cdot Br^-$ signal by only Br^- (a) or $H_2O \cdot Br^-$ (b) does not compensate for the humidity effect. Using the sum of Br^- and $H_2O \cdot Br^-$ (c) for normalization yields a tight correlation to the true I_2 as measured by CE-DOAS, independent of the humidity. The black dashed line indicates the fitted linear calibration.

3.3 Quantification of gas-phase inorganic species

347 Inter-method calibrations and offline calibrations were carried out to quantify the sensitivities of the Br-MION-CIMS
348 to selected calibrants. For the inter-method calibrations, we used the CLOUD chamber as a stable source of I_2 and
349 H_2SO_4, and inter-compared the signals in the Br-MION-CIMS with the CE-DOAS and a pre-calibrated nitrate-CIMS,
350 respectively. For the offline calibrations, we carried out the experiments separately in a laboratory at the University
351 of Helsinki, using permeation tubes to quantify I_2 and Cl_2, and a calibrator to quantify HOI.

352

3.3.1 Inter-method calibrations at CLOUD

3.3.1.1 I_2 calibration using the CE-DOAS

355 As shown in Fig. 3, we use the accurate I_2 time series measured with the CE-DOAS to calibrate normalized I_2 signals
356 in the Br-MION-CIMS. The I_2 concentrations used for the calibration span approximately 2 orders of magnitude,
357 reaching up to 4.6×10^{10} molec cm^{-3}. A linear fit, limited to I_2 concentrations smaller than 10^{10} molec cm^{-3}, establishes
358 the calibration factor as follows:

359 $$[I_2] = 2.7 \times 10^{10} \text{ molec cm}^{-3} \times I_2 \, ^{79}Br^-/(^{79}Br^- + H_2O \, ^{79}Br^-)$$

360 For this range of concentrations, which are typically encountered in the atmosphere, the calibrated Br-MION-CIMS
361 time series agrees within error with the CE-DOAS measurement (1-sigma accuracy 20 %, detection limit 25 pptv for

362   1 min data). Deviations between both time series are generally smaller than 10 % (25 and 75 percentile 0.88 and 1.03,

363   respectively). These small differences may be explained by incomplete homogeneity of iodine concentrations in the

364   chamber and the different sampling positions of CE-DOAS and Br-MION-CIMS.

365

366   **3.3.1.2 H_2SO_4 calibration using a nitrate-CIMS**

367   We derive the H_2SO_4 calibration coefficient for the Br-MION-CIMS using the absolute H_2SO_4 concentrations

368   measured with a pre-calibrated nitrate-CIMS. The calibration protocol of H_2SO_4 in the nitrate-CIMS has been

369   described in detail previously (Kürten et al., 2012). The H_2SO_4 time series used for the inter-method calibration covers

370   a wide concentration range from less than 5.0×10^4 (detection limit of the nitrate-CIMS) to 6.0×10^7 molec cm^{-3}. For

371   Br-MION-CIMS, although both HSO_4^- and H_2SO_4 Br$^-$ appear as distinct peaks for sulfuric acid, we only use the

372   normalized H_2SO_4 $^{79}Br^-$ for the inter-calibration, as HSO_4^- (m/z = 96.96) has substantial interference from the reagent

373   ion H_2O $^{79}Br^-$ (m/z = 96.93). We show in Fig. 4 (a) the linear fit:

374                    $$[H_2SO_4] = 4.1 \times 10^{10} \text{ molec cm}^{-3} \times H_2SO_4 \, ^{79}Br^-/(^{79}Br^- + H_2O \, ^{79}Br^-) - 9.3 \times 10^5)$$

375   The H_2SO_4 calibration coefficient is thus 4.1×10^{10} molec cm^{-3} per normalized signal (cps cps^{-1}), and the correlation

376   coefficient between the two H_2SO_4 traces is 0.95. The systematic 3-sigma accuracy is +50/-33 % for H_2SO_4 calibration

377   using a nitrate-CIMS; detailed accuracy estimation has been discussed previously (Stolzenburg et al., 2020).

378

379   **3.3.2 Offline laboratory calibrations for I_2, Cl_2, and HOI**

380   For the I_2 calibration, we diluted the I_2 flow to seven different values and measured the flow with the Br-MION-CIMS.

381   We repeated the calibration five times; we show the data along with a linear fit between the I_2 concentration and

382   normalized I_2 signal in Fig. 4 (b). The slope of the line gives a calibration coefficient of 6.3×10^{10} molec cm^{-3} per

383   normalized signal (cps cps^{-1}), with R^2 of 0.98 and an overall 1-sigma accuracy of ± 45 %.

384

385   For the Cl_2 calibration, the Cl_2 permeation source was run continuously for 12 hours prior to calibration experiments

386   to ensure complete system equilibrium. A two-stage dilution system similar to the setup of (Gallagher et al., 1997)

387   was set up for diluting the output of the Cl_2 permeation device. The 20 mlpm of N_2 stream emerging from the Cl_2

388   permeation device (operated at room temperature) was diluted in a stream of 6 slpm of dry N_2. Then, a small fraction

389   of this mixture (50 to 300 mlpm) was further mixed with the total flow of 25 slpm of N_2 (20 slpm dry N_2 + 5 slpm

390   humidified N_2) before being sampled by the Br-MION-CIMS. The calibration coefficient for Cl_2 was determined to

391   be 3.5×10^{11} molec cm^{-3} per normalized signal (cps cps^{-1}) from three separate calibration experiments (Fig 4 (c)), with

392   an 1-sigma accuracy of 30 %.

393

394   As for the HOI calibration, we produced a range of HOI concentrations by varying I_2 and OH concentrations in the

395   calibrator. We show in Fig. 4 (d) the linear correlation between the modeled HOI concentrations and measured HOI

396   signals. The slope of the fit corresponds to a calibration coefficient of 3.3×10^{11} molec cm^{-3} per normalized signal (cps

397   cps^{-1}), with an overall 1-sigma accuracy of 55 %. The good correlation (R^2 = 0.97) including various H_2O levels also

398   indicates that H_2O concentrations did not affect the HOI detection.
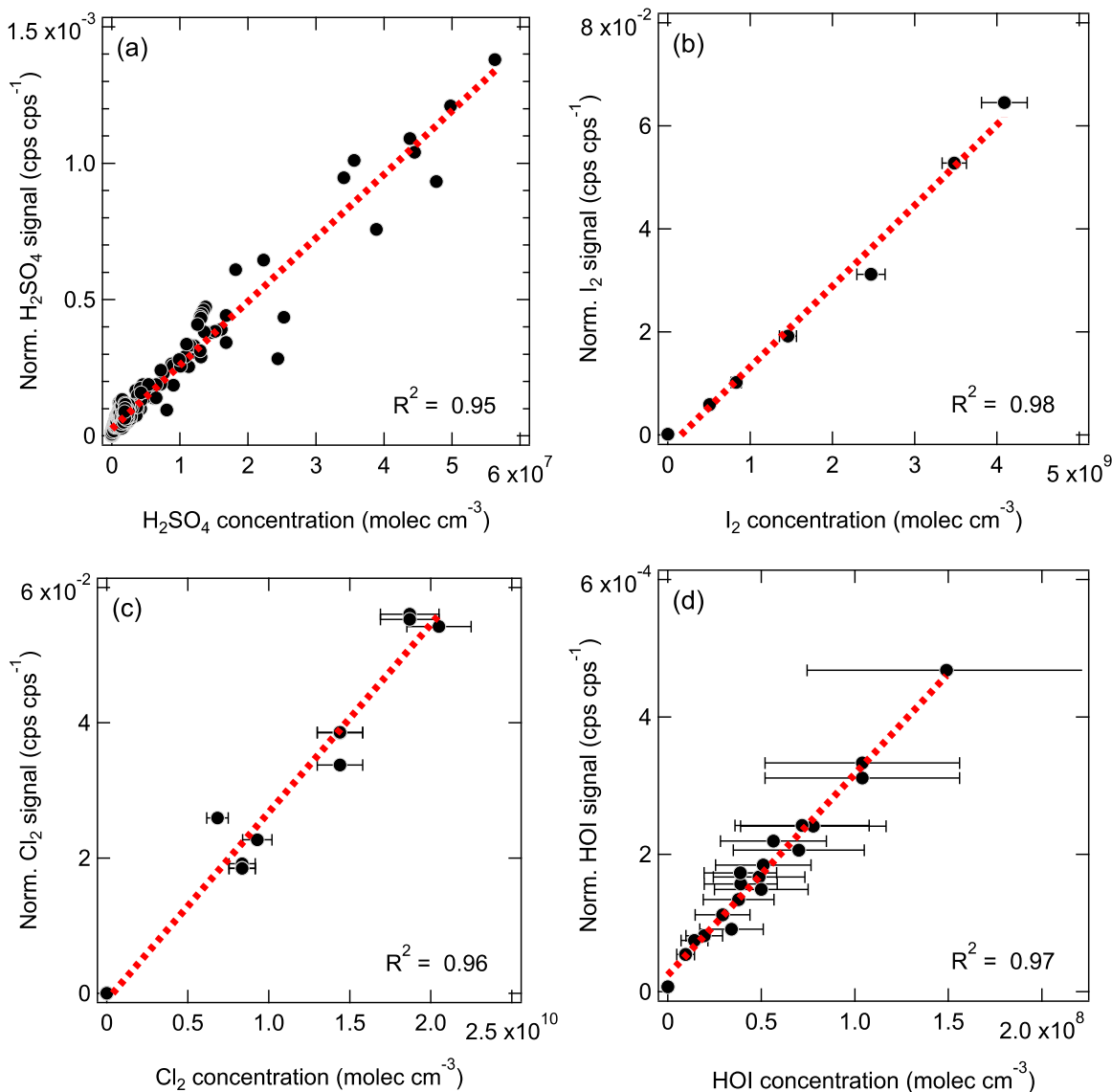
400
Figure 4. The normalized signals (cps cps^{-1}) *vs.* the absolute concentrations (molec cm^{-3}) measured with the Br-MION-CIMS for
(a) H_2SO_4, (b) I_2, (c) Cl_2, and (d) HOI. The red dashed lines are the linear fits. The overall 3-sigma accuracy of +50/-33 % on
[H_2SO_4] is not shown here.

404

3.3.3 Connecting sensitivity to binding enthalpy

Beyond the species for which we carried out calibrations, there are many more, especially iodine species, that cannot
be directly calibrated due to a lack of authentic standards or generation methods. However, the sensitivity of an iodide-
CIMS towards analytes can be predicted by the cluster binding enthalpy, calculated by relatively simple quantum
chemical methods (Iyer et al., 2016). This holds for the Br-CIMS as well. In the instrument, ion clusters, formed from
reactions between analytes and reagent ions, are guided and focused by ion optics during transmission to the detector.
The electric forces applied to the clusters enhance their collision energies with carrier gas molecules. If sufficient
energy is transferred during the collision, cluster fragmentation may occur, affecting the instrument sensitivity for the

413   analytes (Passananti et al., 2019). However, clusters with higher binding enthalpy will be more easily preserved and

414   detected. Analytes that bind to the reagent ions with enthalpies higher than a critical level are likely detected at

415   maximum sensitivity (kinetic-limited detection) by the instrument. For example, the calculated critical enthalpy is 25

416   kcal mol^{-1} for the iodide-CIMS used in Iyer et al. (Iyer et al., 2016) and Lopez-Hilfiker et al. (Lopez-Hilfiker et al.,

417   2016), calculated at the DLPNO-CCSD(T)/def2-QZVPP//PBE/aug-cc-pVTZ-PP level of theory.

418

419   For the bromide chemical ionization, there are two types of fragmentation pathways:

420   1)   Reversion to the original form of Br$^-$ and analyte

421   X-H Br$^-$ $\rightarrow$ X-H + Br$^-$ (1)

422   2)   Proton transfer from the analyte to Br$^-$

423   X-H Br$^-$ $\rightarrow$ X$^-$ + HBr   (2)

424   where the X-H is the hydrogen bond donor. An analyte should be detected at the maximum sensitivity when the

425   dissociation enthalpy for the first pathway is either a) much higher than the critical enthalpy (dissociation of X-H Br$^-$

426   to X-H and Br$^-$ does not occur), or b) lower than the critical enthalpy, but much higher than that of the second pathway

427   (dissociation of X-H Br$^-$ to X-H and Br$^-$ may occur, but dissociation to X$^-$ and HBr is the dominant pathway). Whether

428   the enthalpy for the second pathway is higher than the critical enthalpy does not directly affect the sensitivity, as both

429   X-H Br$^-$ and X$^-$ can be measured and counted. The sensitivity toward X-H would be reduced only when the first

430   reversion pathway occurs to a non-negligible extent. Taking H_2SO_4 as an example, the dissociation enthalpies for the

431   first and second pathways are 41.1 and 27.9 kcal mol^{-1}, respectively. If some of the H_2SO_4 Br$^-$ dissociate, they

432   preferably become HSO_4^- and are detectable by the Br-CIMS. Thus, H_2SO_4 can be detected at the maximum sensitivity.

433

434   While we were unable to experimentally establish a correlation between sensitivities and binding enthalpies due to

435   limited quantifiable halogen species, we can predict the tentative critical enthalpy as the binding enthalpy of a species

436   that is likely detected at the maximum sensitivity. We list the cluster formation enthalpies for a selection of halogen

437   containing species in Table 1 and the corresponding cluster dissociation enthalpies in Table 2. Among all the

438   calibration coefficients listed in Table 3, H_2SO_4 and I_2 have the lowest calibration coefficients (highest sensitivities).

439   Thereby, we conclude that both H_2SO_4 and I_2 are detected at the maximum sensitivity, suggesting a critical enthalpy

440   not higher than 33.7 kcal mol^{-1}. We can then infer the sensitivity for other species that are difficult to calibrate by

441   comparing their binding enthalpies to those of the benchmark species. For example, ICl and IBr should have the

442   maximum sensitivity, since the dissociation enthalpies for ICl Br$^-$ and IBr Br$^-$ are both much higher than 33.7 kcal

443   mol^{-1} (Table 2). Although HIO_3 Br$^-$ has a lower dissociation enthalpy than the critical value, the favored dissociation

444   pathway is proton transfer (the second pathway); HIO_3 can thus be considered as a maximum sensitivity species

445   detectable as IO_3^- ions after proton transfer. This is consistent with the fact that both HIO_3 Br$^-$ and IO_3^- are detected in

446   Figure 1, so is the case with H_2SO_4. We thus assume that HIO_3 has a kinetic calibration coefficient of 4.1×10^{10} molec

447   cm^{-3} cps cps^{-1}, the value for H_2SO_4. However, the lowest dissociation enthalpies of HOI Br$^-$ and Cl_2 Br$^-$ are 26.9 and

448   22.3 kcal mol^{-1}, respectively, consistent with their higher calibration coefficients of 3.3×10^{11} and 3.5×10^{11} molec cm$^-$

449   ^{3} cps cps^{-1}. The dissociation enthalpies for IO Br$^-$, OIO Br$^-$, and HIO_2 Br$^-$ are 24.5, 23.2, and 29.2 kcal mol^{-1},

450 respectively. We would expect that their sensitives are lower than the maximum sensitivity. Since the dissociation

451 enthalpies for IO Br$^-$ and OIO Br$^-$ are between those of HOI Br$^-$ and Cl$_2$ Br$^-$, a similar calibration coefficient may be

452 applied, but direct calibrations are more preferable. We note that when transferring the calibration factor from one

453 species to another, the diffusivity difference should be accounted, since it affects the inlet line loss. This factor is not

454 considered in the cluster enthalpies calculations.

455

456 Further, we estimate the detection limit of the calibrated species. The detection limit is defined as the analyte

457 concentration, corresponding to the sum of the mean signal and three times the standard deviations (3σ) of the

458 background fluctuations during a two-hour background measurement. We derive the detection limit of HOI, HIO$_3$, I$_2$,

459 and H$_2$SO$_4$ to be 5.8×10^6, 1.2×10^5, 3.8×10^5, and 2.0×10^5 molec cm^{-3} (or 0.2, 0.005, 0.015, and 0.008 pptv), respectively,

460 for a 2-min integration time.

461

462 **3.4 Comparison between Br-MION-CIMS and Br-FIGAERO-CIMS**

463 While Br-MION-CIMS and Br-FIGAERO-CIMS use the same chemical ionization scheme, their designs differ in the

464 ion-molecule reaction chamber (IMR). MION is an atmospheric pressure (1 bar) drift tube; analyte molecules gain an

465 electric charge in an axial laminar flow. FIGAERO is connected to a cone-shaped IMR chamber operated at a reduced

466 pressure (150 mbar); the sample flow is injected into the inlet via an orifice, necessarily causing turbulence and wall

467 interactions in the IMR region. The atmospheric pressure and reduced pressure IMRs are both widely used for trace

468 gas measurements. We thus compare iodine species measurements from Br-MION-CIMS and Br-FIGAERO-CIMS,

469 to better understand the performance and applicability of the bromide ionization scheme.

470

471 We show in Fig. 5 the same iodine oxidation event as in Fig. 2, to illustrate the time series for HIO$_3$ Br$^-$, HOI Br$^-$,

472 IO Br$^-$, and I$_2$ Br$^-$, measured with Br-MION-CIMS (red circles) and Br-FIGAERO-CIMS (grey sticks), respectively.

473 Note that the FIGAERO alternates between gas and particle measurements; here we show only the gas-phase signals.

474 Clear and concurrent signals of HIO$_3$, HOI, IO, and I$_2$ are evident from both the Br-MION-CIMS and Br-FIGAERO-

475 CIMS. Prior to the iodine oxidation event (08:11), there was no photochemical production and thus virtually no signal

476 of oxidized iodine species in both instruments. The dark reaction of ozone with I$_2$ did not proceed at a significant rate,

477 due to the low rate coefficient and to low levels of I$_2$. Signals detected during this period are considered as the persistent

478 background, coming from electronic noise or other sources such as the ionizer, carrier flows, or long-term "memory"

479 in the case of the Br-FIGAERO-CIMS. Not surprisingly, the Br-MION-CIMS has a near-zero background for all

480 analytes. For HIO$_3$ (Fig. 5 (a)), the background signal in the Br-FIGAERO-CIMS is also negligible; however, IO

481 shows a substantial persistent background (Fig. 5 (c)) in the Br-FIGAERO-CIMS.

482

483 When we initiated the photochemistry, oxidized iodine signals rapidly built up toward an asymptote within timescales

484 of minutes. The instrumental differences in these timescales are small for HIO$_3$ and HOI, but larger for IO. When

485 colliding with the IMR surface, HIO$_3$ condenses irreversibly; it thus makes sense that the Br-MION-CIMS and Br-

486 FIGAERO-CIMS signals show the same timescale for HIO$_3$. Semi-volatile HOI, however, can return to the gas phase

from the walls depending on the surface coverage of HOI and the vapor concentration. Additionally, the heterogeneous reaction of aqueous iodide (I^-) and ozone (Carpenter et al., 2013) could also contribute to the emission of HOI from the IMR wall in the FIGAERO. As the evaporation flux is typically a function of the amount analyte on the surface, the buffering effect could degrade the instrument time response upon changes in analyte concentration. Here, however, we did not observe a significant memory effect, likely because the HOI concentration was too low to fully saturate the IMR surface or because any HOI evaporation was suppressed due to an enhanced accommodation coefficient of HOI on the metal surface. We expect IO to be prone to loss on the metal surface due to its radical nature.

After the iodine oxidation event (10:21), the photochemical production of oxidized iodine species was terminated and vapor concentrations decayed exponentially due to dilution and losses to chamber walls. Memory effects could also influence the signal time constant. The dilution loss rate was around 2.1×10^{-4} s^{-1} (4760 s time constant) for all species in the chamber, determined by the total chamber flow rate and the chamber volume. Wall loss rates, however, vary for species with different diffusion constants. The decay rates of HIO_3 are 400 s for the Br-MION-CIMS and 370 s for the Br-FIGAERO-CIMS, much faster than the dilution loss. For comparison, the time constant for H_2SO_4 vapor loss was 300 s. These time constants are thus consistent with wall loss (around 2.2×10^{-3} s^{-1}). The IO decay time constant is 294 s for the Br-MION-CIMS and 435 s for the Br-FIGAERO-CIMS. The time constant for the Br-MION-CIMS indicates that the decay of IO is also driven by wall loss, so the net flux during this period was thus towards the wall rather than from the wall. Therefore, the difference of IO between instruments may well be attributed to the persistent background from the ionizer of the FIGAERO. The HOI signals have longer decay time constants in both instruments of 909 s for the Br-MION-CIMS and 714 s for the Br-FIGAERO-CIMS; this may reflect a time constant for depletion of HOI adsorbed to the chamber walls. The I_2 signal increases after the event termination because it is no longer photolyzed while its injection continues.

Applying the calibration coefficients, we convert the Br-MION-CIMS signals to absolute concentrations, and subsequently correlate them with signals measured with Br-FIGAERO-CIMS. We then estimate the tentative detection limits for HOI and HIO_3 in the Br-FIGAERO-CIMS to be 3.3×10^7 and 5.1×10^6 molec cm^{-3} (versus 5.8×10^6 and 1.2×10^5 molec cm^{-3} in the Br-MION-CIMS), respectively, at 3σ of the background signal for a 2-min integration time during a two-hour period; they are in general one order of magnitude higher than those in the Br-MION-CIMS. This is in line with the higher background signals observed in the Br-FIGAERO-CIMS. Note that for both HOI and HIO_3 the uncertainties introduced from the correlational analysis are negligible compared to the limited accuracy of the calibration sources (55 % for HOI and +50/-33 % for HIO_3). We are unable to estimate the I_2 detection limit in the Br-FIGAREO-CIMS, due to a lack of I_2 background measurement; but Br-FIGAERO-CIMS can and did detect I_2 at the low pptv level with good fidelity.
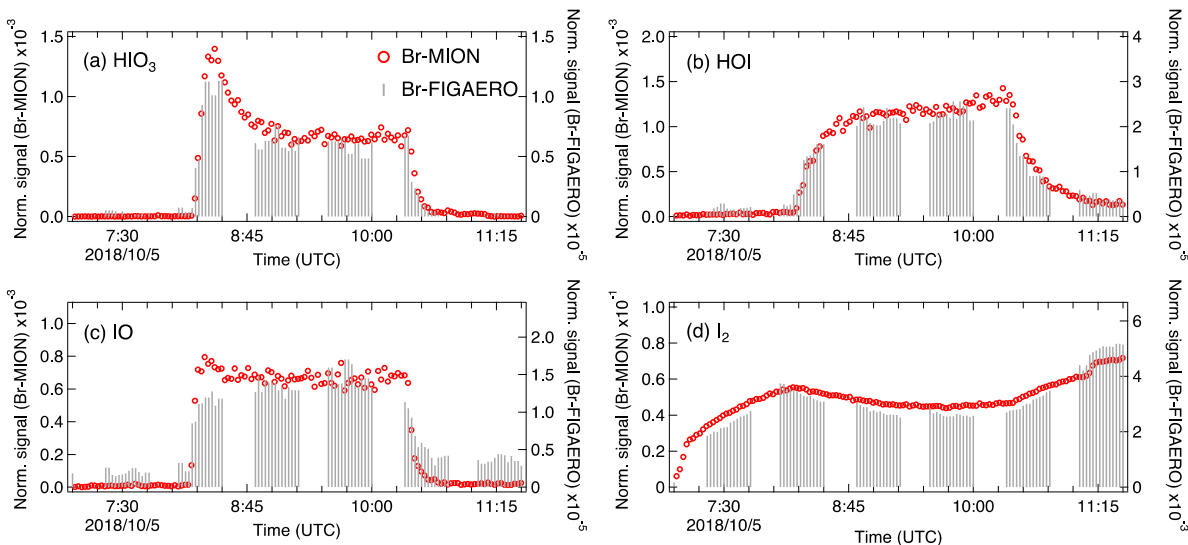
Figure 5. Signal comparison of selected iodine species measured with Br-MION-CIMS and (gas-phase) Br-FIGAERO-CIMS, respectively, during the same iodine oxidation experiment shown in Fig. 2.

4 Summary and conclusion

We confirm in this study that bromide chemical ionization is a suitable technique for the time-resolved, highly sensitive, and simultaneous measurements of iodine species and sulfuric acid. The Br-MION-CIMS shows constant sensitivity throughout the relative humidity range of 40 to 80 % at -10 ℃, as long as the sum of the two reagent ions $(Br^- + H_2O \cdot Br^-)$ is used for signal normalization. This demonstrates the applicability of this technique to field measurements in the ambient marine environment.

We quantify iodine species and sulfuric acid via offline calibrations (i.e. permeation tube and calibrator) and inter-method calibrations (i.e. CE-DOAS and pre-calibrated nitrate-CIMS. Further, we calculate the binding enthalpies between the calibrated species and reagent ions, which qualitatively agree with the corresponding calibration coefficients. This indicates that the quantum chemical calculations can be employed along with the calibration experiments to determine the sensitivities for unquantifiable species; more work is required to further establish the correlation between calibration coefficients and binding enthalpies.

Further, using inter-method and offline calibrations, we estimate the detection limits of HOI, HIO$_3$, I$_2$, and H$_2$SO$_4$ in Br-MION-CIMS being 5.8×10^6, 1.2×10^5, 3.8×10^5, and 2.0×10^5 molec cm^{-3}, respectively, for a 2-min integration time during a two-hour period. To our knowledge, the simultaneous measurements of various iodine species and sulfuric acid with low detection limits are unprecedented for online techniques. Detection limits for HOI and HIO$_3$ in the Br-FIGAERO-CIMS are 3.3×10^7 and 5.1×10^6 molec cm^{-3}, which are in general one order of magnitude higher than those in the Br-MION-CIMS. The signal comparison between the two instruments also shows that the Br-CIMS can be coupled to both the atmospheric pressure and the reduced pressure interfaces for iodine species and sulfuric acid measurements in the marine environment.

548
549 *Data availability.* Data available on request from the authors.

550

551 *Author Contributions.* M.W., X.-C.H., Y.-J.T and H.F. wrote the manuscript. X.-C.H., Y.-J.T., M.W. and M.Sip.
552 designed the experiments. X.-C.H., Y.-J.T. and J.S. carried out the Br-MION-CIMS measurements, M.W., D.C. and
553 V.H. carried out the Br-FIGAERO-CIMS measurements, and H.F. carried out the CE-DOAS measurements. Y.-J.T.,
554 X.-C.H., H.F., D.C., J.S. and M.Sim. performed the calibrations. S.I., X.-C.H. and T.K. carried out the quantum
555 chemical calculations. M.W. performed the comparison analysis of the Br-FIGAERO-CIMS and Br-MION-CIMS.
556 N.-M.D., T.K., M.R., R.V. and M.Sip. commented on the manuscript. All other co-authors participated in either the
557 development and preparations of the CLOUD facility and the instruments, and/or collecting and analyzing the data.

558

559 *Competing interests.* The authors declare that they have no conflict of interest.

560

561 *Acknowledgement.* We thank the European Organization for Nuclear Research (CERN) for supporting CLOUD with
562 important technical and financial resources and for providing a particle beam from the CERN Proton Synchrotron.
563 We also thank Juhani Virkanen and Heini Ali-Kovero for providing assistance in the laboratory analytical experiments.

564

565 *Financial support.* This research has received funding from the US National Science Foundation (AGS-1531284,
566 AGS-1801574 and AGS-1801280), Academy of Finland (projects: 296628, 328290, Centre of Excellence 1118615)
567 and the European Research Council (ERC) under the European Union's Horizon 2020 research and innovation
568 programme (GASPARCON, grant agreement no. 714621). The FIGAERO-CIMS was supported by an MRI grant for
569 the US NSF AGS-1531284 as well as the Wallace Research Foundation.

570

571 **References**
572 Bitter, M., Ball, S. M., Povey, I. M. and Jones, R. L.: A broadband cavity ringdown spectrometer for in-situ
573 measurements of atmospheric trace gases, Atmos. Chem. Phys., doi:10.5194/acp-5-2547-2005, 2005.

574 Carpenter, L. J., MacDonald, S. M., Shaw, M. D., Kumar, R., Saunders, R. W., Parthipan, R., Wilson, J. and Plane,
575 J. M. C.: Atmospheric iodine levels influenced by sea surface emissions of inorganic iodine, Nat. Geosci.,
576 doi:10.1038/ngeo1687, 2013.

577 Chai, J. Da and Head-Gordon, M.: Long-range corrected hybrid density functionals with damped atom-atom
578 dispersion corrections, Phys. Chem. Chem. Phys., doi:10.1039/b810189b, 2008.

579 Chance, R. J., Shaw, M., Telgmann, L., Baxter, M. and Carpenter, L. J.: A comparison of spectrophotometric and
580 denuder based approaches for the determination of gaseous molecular iodine, Atmos. Meas. Tech., doi:10.5194/amt-
581 3-177-2010, 2010.

582 Dias, A., Ehrhart, S., Vogel, A., Mathot, S., Onnela, A., Almeida, J., Kirkby, J., Williamson, C. and Mumford, S.:
583 Temperature uniformity in the CERN CLOUD chamber, Atmos. Meas. Tech., 10, 5075–5088, 2017.

584 Dillon, T. J., Tucceri, M. E. and Crowley, J. N.: Laser induced fluorescence studies of iodine oxide chemistry: Part
585 II. The reactions of IO with CH3O2, CF3O2 and O3, Phys. Chem. Chem. Phys., doi:10.1039/b611116e, 2006.

586 Duplissy, J., Merikanto, J., Franchin, A., Tsagkogeorgas, G., Kangasluoma, J., Wimmer, D., Vuollekoski, H.,
587 Schobesberger, S., Lehtipalo, K., Flagan, R. C., Brus, D., Donahue, N. M., Vehkamaki, H., Almeida, J., Amorim,
588 A., Barmet, P., Bianchi, F., Breitenlechner, M., Dunne, E. M., Guida, R., Henschel, H., Junninen, H., Kirkby, J.,
589 Kurten, A., Kupc, A., Maattanen, A., Makhmutov, V., Mathot, S., Nieminen, T., Onnela, A., Praplan, A. P.,
590 Riccobono, F., Rondo, L., Steiner, G., Tome, A., Walther, H., Baltensperger, U., Carslaw, K. S., Dommen, J.,
591 Hansel, A., Petaja, T., Sipila, M., Stratmann, F., Vrtala, A., Wagner, P. E., Worsnop, D. R., Curtius, J. and Kulmala,
592 M.: Effect of ions on sulfuric acid-water binary particle formation: 2. Experimental data and comparison with QC-
593 normalized classical nucleation theory, J. Geophys. Res., 121, 1752–1775, doi:10.1002/2015JD023539, 2016.

594 Feller, D.: The role of databases in support of computational chemistry calculations, J. Comput. Chem.,

595   doi:10.1002/(SICI)1096-987X(199610)17:13<1571::AID-JCC9>3.0.CO;2-P, 1996.

596   Finley, B. D. and Saltzman, E. S.: Observations of Cl2, Br2, and I2 in coastal marine air, J. Geophys. Res. Atmos.,
597   doi:10.1029/2008JD010269, 2008.

598   Frisch, M. J., Trucks, G. W., Schlegel, H. B., Scuseria, G. E., Robb, M. A., Cheeseman, J. R., Scalmani, G., Barone,
599   V., Mennucci, B., Petersson, G. A., Nakatsuji, H., Caricato, M., Li, X., Hratchian, H. P., Izmaylov, A. F., Bloino, J.,
600   Zheng, G., Sonnenberg, J. L., Hada, M., Ehara, M., Toyota, K., Fukuda, R., Hasegawa, J., Ishida, M., Nakajima, T.,
601   Honda, Y., Kitao, O., Nakai, H., Vreven, T., Montgomery Jr., J. A., Peralta, J. E., Ogliaro, F., Bearpark, M., Heyd, J.
602   J., Brothers, E., Kudin, K. N., Staroverov, V. N., Kobayashi, R., Normand, J., Raghavachari, K., Rendell, A.,
603   Burant, J. C., Iyengar, S. S., Tomasi, J., Cossi, M., Rega, N., Millam, J. M., Klene, M., Knox, J. E., Cross, J. B.,
604   Bakken, V., Adamo, C., Jaramillo, J., Gomperts, R., Stratmann, R. E., Yazyev, O., Austin, A. J., Cammi, R.,
605   Pomelli, C., Ochterski, J. W., Martin, R. L., Morokuma, K., Zakrzewski, V. G., Voth, G. A., Salvador, P.,
606   Dannenberg, J. J., Dapprich, S., Daniels, A. D., Farkas, �., Foresman, J. B., Ortiz, J. V, Cioslowski, J. and Fox, D.
607   J.: Gaussian09 Revision D.01, Gaussian Inc. Wallingford CT, Gaussian 09 Revis. C.01, 2010.

608   Gallagher, M. S., King, D. B., Whung, P. Y. and Saltzman, E. S.: Performance of the HPLC/fluorescence SO2
609   detector during the GASIE instrument intercomparison experiment, J. Geophys. Res. Atmos.,
610   doi:10.1029/97jd00700, 1997.

611   Gómez Martín, J. C., Blahins, J., Gross, U., Ingham, T., Goddard, A., Mahajan, A. S., Ubelis, A. and Saiz-Lopez,
612   A.: In situ detection of atomic and molecular iodine using Resonance and Off-Resonance Fluorescence by Lamp
613   Excitation: ROFLEX, Atmos. Meas. Tech., doi:10.5194/amt-4-29-2011, 2011.

614   Gómez Martín, J. C., Gálvez, O., Baeza-Romero, M. T., Ingham, T., Plane, J. M. C. and Blitz, M. A.: On the
615   mechanism of iodine oxide particle formation, Phys. Chem. Chem. Phys., doi:10.1039/c3cp51217g, 2013.

616   He, X.-C., Iyer, S., Sipilä, M., Ylisirniö, A., Peltola, M., Kontkanen, J., Baalbaki, R., Simon, M., Kürten, A., Tham,
617   Y. J., Pesonen, J., Ahonen, L. R., Amanatidis, S., Amorim, A., Baccarini, A., Beck, L., Bianchi, F., Brilke, S., Chen,
618   D., Chiu, R., Curtius, J., Dada, L., Dias, A., Dommen, J., Donahue, N. M., Duplissy, J., El Haddad, I., Finkenzeller,
619   H., Fischer, L., Heinritzi, M., Hofbauer, V., Kangasluoma, J., Kim, C., Koenig, T. K., Kubečka, J., Kvashnin, A.,
620   Lamkaddam, H., Lee, C. P., Leiminger, M., Li, Z., Makhmutov, V., Xiao, M., Marten, R., Nie, W., Onnela, A.,
621   Partoll, E., Petäjä, T., Salo, V.-T., Schuchmann, S., Steiner, G., Stolzenburg, D., Stozhkov, Y., Tauber, C., Tomé,
622   A., Väisänen, O., Vazquez-Pufleau, M., Volkamer, R., Wagner, A. C., Wang, M., Wang, Y., Wimmer, D., Winkler,
623   P. M., Worsnop, D. R., Wu, Y., Yan, C., Ye, Q., Lehtinen, K., Nieminen, T., Manninen, H. E., Rissanen, M.,
624   Schobesberger, S., Lehtipalo, K., Baltensperger, U., Hansel, A., Kerminen, V.-M., Flagan, R. C., Kirkby, J., Kurtén,
625   T. and Kulmala, M.: Determination of the collision rate coefficient between charged iodic acid clusters and iodic
626   acid using the appearance time method, Aerosol Sci. Technol., 55(2), 231–242,
627   doi:10.1080/02786826.2020.1839013, 2021a.

628   He, X.-C., Tham, Y. J., Dada, L., Wang, M., Finkenzeller, H., Stolzenburg, D., Iyer, S., Simon, M., Kürten, A.,
629   Shen, J. and others: Role of iodine oxoacids in atmospheric aerosol nucleation, Science (80-.)., 371(6529), 589–
630   595, 2021b.

631   He, X.: From the measurement of halogenated species to iodine particle formation, 2017.

632   Iyer, S., Lopez-Hilfiker, F., Lee, B. H., Thornton, J. A. and Kurtén, T.: Modeling the Detection of Organic and
633   Inorganic Compounds Using Iodide-Based Chemical Ionization, J. Phys. Chem. A, doi:10.1021/acs.jpca.5b09837,
634   2016.

635   Junninen, H., Ehn, M., Petaja, T., Luosujarvi, L., Kotiaho, T., Kostiainen, R., Rohner, U., Gonin, M., Fuhrer, K.,
636   Kulmala, M., Worsnop, D. R., Petäjä, T., Luosujärvi, L., Kotiaho, T., Kostiainen, R., Rohner, U., Gonin, M., Fuhrer,
637   K., Kulmala, M. and Worsnop, D. R.: A high-resolution mass spectrometer to measure atmospheric ion composition,
638   Atmos. Meas. Tech., 3(4), 1039–1053, doi:10.5194/amt-3-1039-2010, 2010.

639   Kazantseva, N. N., Ernepesova, A., Khodjamamedov, A., Geldyev, O. A. and Krumgalz, B. S.: Spectrophotometric
640   analysis of iodide oxidation by chlorine in highly mineralized solutions, in Analytica Chimica Acta., 2002.

641   Kendall, R. A., Dunning, T. H. and Harrison, R. J.: Electron affinities of the first-row atoms revisited. Systematic
642   basis sets and wave functions, J. Chem. Phys., doi:10.1063/1.462569, 1992.

643   Kercher, J. P., Riedel, T. P. and Thornton, J. A.: Chlorine activation by N2O5: Simultaneous, in situ detection of

644 ClNO2 and N2O5 by chemical ionization mass spectrometry, Atmos. Meas. Tech., doi:10.5194/amt-2-193-2009,
645 2009.

646 Kirkby, J., Curtius, J., Almeida, J., Dunne, E., Duplissy, J., Ehrhart, S., Franchin, A., Gagné, S., Ickes, L., Kürten,
647 A., Kupc, A., Metzger, A., Riccobono, F., Rondo, L., Schobesberger, S., Tsagkogeorgas, G., Wimmer, D., Amorim,
648 A., Bianchi, F., Breitenlechner, M., David, A., Dommen, J., Downard, A., Ehn, M., Flagan, R. C., Haider, S.,
649 Hansel, A., Hauser, D., Jud, W., Junninen, H., Kreissl, F., Kvashin, A., Laaksonen, A., Lehtipalo, K., Lima, J.,
650 Lovejoy, E. R., Makhmutov, V., Mathot, S., Mikkilä, J., Minginette, P., Mogo, S., Nieminen, T., Onnela, A.,
651 Pereira, P., Petäjä, T., Schnitzhofer, R., Seinfeld, J. H., Sipilä, M., Stozhkov, Y., Stratmann, F., Tomé, A.,
652 Vanhanen, J., Viisanen, Y., Vrtala, A., Wagner, P. E., Walther, H., Weingartner, E., Wex, H., Winkler, P. M.,
653 Carslaw, K. S., Worsnop, D. R., Baltensperger, U. and Kulmala, M.: Role of sulphuric acid, ammonia and galactic
654 cosmic rays in atmospheric aerosol nucleation, Nature, 476, 429 [online] Available from:
655 https://doi.org/10.1038/nature10343, 2011.

656 Kirkby, J., Duplissy, J., Sengupta, K., Frege, C., Gordon, H., Williamson, C., Heinritzi, M., Simon, M., Yan, C.,
657 Almeida, J., Trostl, J., Nieminen, T., Ortega, I. K., Wagner, R., Adamov, A., Amorim, A., Bernhammer, A. K.,
658 Bianchi, F., Breitenlechner, M., Brilke, S., Chen, X. M., Craven, J., Dias, A., Ehrhart, S., Flagan, R. C., Franchin,
659 A., Fuchs, C., Guida, R., Hakala, J., Hoyle, C. R., Jokinen, T., Junninen, H., Kangasluoma, J., Kim, J., Krapf, M.,
660 Kurten, A., Laaksonen, A., Lehtipalo, K., Makhmutov, V., Mathot, S., Molteni, U., Onnela, A., Perakyla, O., Piel,
661 F., Petaja, T., Praplan, A. P., Pringle, K., Rap, A., Richards, N. A. D. D., Riipinen, I., Rissanen, M. P., Rondo, L.,
662 Sarnela, N., Schobesberger, S., Scott, C. E., Seinfeld, J. H., Sipila, M., Steiner, G., Stozhkov, Y., Stratmann, F.,
663 Tome, A., Virtanen, A., Vogel, A. L., Wagner, A. C., Wagner, P. E., Weingartner, E., Wimmer, D., Winkler, P. M.,
664 Ye, P. L., Zhang, X., Hansel, A., Dommen, J., Donahue, N. M., Worsnop, D. R., Baltensperger, U., Kulmala, M.,
665 Carslaw, K. S., Curtius, J., Tomé, A., Virtanen, A., Vogel, A. L., Wagner, A. C., Wagner, P. E., Weingartner, E.,
666 Wimmer, D., Winkler, P. M., Ye, P. L., Zhang, X., Hansel, A., Dommen, J., Donahue, N. M., Worsnop, D. R.,
667 Baltensperger, U., Kulmala, M., Carslaw, K. S. and Curtius, J.: Ion-induced nucleation of pure biogenic particles,
668 Nature, 533(7604), 521–526, doi:10.1038/nature17953, 2016.

669 Koenig, T. K., Baidar, S., Campuzano-Jost, P., Cuevas, C. A., Dix, B., Fernandez, R. P., Guo, H., Hall, S. R.,
670 Kinnison, D., Nault, B. A., Ullmann, K., Jimenez, J. L., Saiz-Lopez, A. and Volkamer, R.: Quantitative detection of
671 iodine in the stratosphere, Proc. Natl. Acad. Sci. U. S. A., doi:10.1073/pnas.1916828117, 2020.

672 Kurten, A., Rondo, L., Ehrhart, S. and Curtius, J.: Calibration of a Chemical Ionization Mass Spectrometer for the
673 Measurement of Gaseous Sulfuric Acid, J. Phys. Chem. A, 116, 6375–6386, doi:Doi 10.1021/Jp212123n, 2012.

674 Lawler, M. J., Sander, R., Carpenter, L. J., Lee, J. D., Von Glasow, R., Sommariva, R. and Saltzman, E. S.: HOCl
675 and Cl2 observations in marine air, Atmos. Chem. Phys., doi:10.5194/acp-11-7617-2011, 2011.

676 Lee, B. H., Lopez-Hilfiker, F. D., Mohr, C., Kurten, T., Worsnop, D. R. and Thornton, J. A.: An iodide-adduct high-
677 resolution time-of-flight chemical-ionization mass spectrometer: application to atmospheric inorganic and organic
678 compounds, Env. Sci Technol, 48(11), 6309–6317, doi:10.1021/es500362a, 2014.

679 Lee, B. H., Lopez-Hilfiker, F. D., Veres, P. R., McDuffie, E. E., Fibiger, D. L., Sparks, T. L., Ebben, C. J., Green, J.
680 R., Schroder, J. C., Campuzano-Jost, P., Iyer, S., D'Ambro, E. L., Schobesberger, S., Brown, S. S., Wooldridge, P.
681 J., Cohen, R. C., Fiddler, M. N., Bililign, S., Jimenez, J. L., Kurtén, T., Weinheimer, A. J., Jaegle, L. and Thornton,
682 J. A.: Flight Deployment of a High-Resolution Time-of-Flight Chemical Ionization Mass Spectrometer:
683 Observations of Reactive Halogen and Nitrogen Oxide Species, J. Geophys. Res. Atmos.,
684 doi:10.1029/2017JD028082, 2018.

685 Leigh, R. J., Ball, S. M., Whitehead, J., Leblanc, C., Shillings, A. J. L., Mahajan, A. S., Oetjen, H., Lee, J. D., Jones,
686 C. E., Dorsey, J. R., Gallagher, M., Jones, R. L., Plane, J. M. C., Potin, P. and McFiggans, G.: Measurements and
687 modelling of molecular iodine emissions, transport and photodestruction in the coastal region around Roscoff,
688 Atmos. Chem. Phys., doi:10.5194/acp-10-11823-2010, 2010.

689 Lopez-Hilfiker, F. D., Mohr, C., Ehn, M., Rubach, F., Kleist, E., Wildt, J., Mentel, T. F., Lutz, A., Hallquist, M.,
690 Worsnop, D. and Thornton, J. A.: A novel method for online analysis of gas and particle composition: description
691 and evaluation of a Filter Inlet for Gases and AEROsols (FIGAERO), Atmos. Meas. Tech., 7(4), 983–1001,
692 doi:10.5194/amt-7-983-2014, 2014.

693 Lopez-Hilfiker, F. D., Iyer, S., Mohr, C., Lee, B. H., D'ambro, E. L., Kurtén, T. and Thornton, J. A.: Constraining
694 the sensitivity of iodide adduct chemical ionization mass spectrometry to multifunctional organic molecules using

695 the collision limit and thermodynamic stability of iodide ion adducts, Atmos. Meas. Tech., doi:10.5194/amt-9-1505-
696 2016, 2016.

697 Marcy, T. P., Fahey, D. W., Gao, R. S., Popp, P. J., Richard, E. C., Thompson, T. L., Rosenlof, K. H., Ray, E. A.,
698 Salawitch, R. J., Atherton, C. S., Bergmann, D. J., Ridley, B. A., Weinheimer, A. J., Loewenstein, M., Weinstock, E.
699 M. and Mahoney, M. J.: Quantifying Stratospheric Ozone in the Upper Troposphere with in Situ Measurements of
700 HCl, Science (80-.)., doi:10.1126/science.1093418, 2004.

701 McFiggans, G., Coe, H., Burgess, R., Allan, J., Cubison, M., Alfarra, M. R., Saunders, R., Saiz-Lopez, A., Plane, J.
702 M. C., Wevill, D. J., Carpenter, L. J., Rickard, A. R. and Monks, P. S.: Direct evidence for coastal iodine particles
703 from Laminaria macroalgae - Linkage to emissions of molecular iodine, Atmos. Chem. Phys., doi:10.5194/acp-4-
704 701-2004, 2004.

705 Meinen, J., Thieser, J., Platt, U. and Leisner, T.: Technical Note: Using a high finesse optical resonator to provide a
706 long light path for differential optical absorption spectroscopy: CE-DOAS, Atmos. Chem. Phys., doi:10.5194/acp-
707 10-3901-2010, 2010.

708 Neese, F.: The ORCA program system, Wiley Interdiscip. Rev. Comput. Mol. Sci., doi:10.1002/wcms.81, 2012.

709 O'dowd, C. D., Jimenez, J. L., Bahreini, R., Flagan, R. C., Seinfeld, J. H., Hämerl, K., Pirjola, L., Kulmala, M. and
710 Hoffmann, T.: Marine aerosol formation from biogenic iodine emissions, Nature, doi:10.1038/nature00775, 2002.

711 Passananti, M., Zapadinsky, E., Zanca, T., Kangasluoma, J., Myllys, N., Rissanen, M. P., Kurtén, T., Ehn, M.,
712 Attoui, M. and Vehkamäki, H.: How well can we predict cluster fragmentation inside a mass spectrometer?, Chem.
713 Commun., doi:10.1039/c9cc02896j, 2019.

714 Pfeifer, J., Simon, M., Heinritzi, M., Piel, F., Weitz, L., Wang, D., Granzin, M., Müller, T., Bräkling, S., Kirkby, J.,
715 Curtius, J. and Kürten, A.: Measurement of ammonia, amines and iodine compounds using protonated water cluster
716 chemical ionization mass spectrometry, Atmos. Meas. Tech., doi:10.5194/amt-13-2501-2020, 2020.

717 Prados-Roman, C., Cuevas, C. A., Fernandez, R. P., Kinnison, D. E., Lamarque, J. F. and Saiz-Lopez, A.: A
718 negative feedback between anthropogenic ozone pollution and enhanced ocean emissions of iodine, Atmos. Chem.
719 Phys., doi:10.5194/acp-15-2215-2015, 2015.

720 Raso, A. R. W., Custard, K. D., May, N. W., Tanner, D., Newburn, M. K., Walker, L., Moore, R. J., Huey, L. G.,
721 Alexander, L., Shepson, P. B. and Pratt, K. A.: Active molecular iodine photochemistry in the Arctic, Proc. Natl.
722 Acad. Sci. U. S. A., doi:10.1073/pnas.1702803114, 2017.

723 Riplinger, C. and Neese, F.: An efficient and near linear scaling pair natural orbital based local coupled cluster
724 method, J. Chem. Phys., doi:10.1063/1.4773581, 2013.

725 Rissanen, M. P., Mikkilä, J., Iyer, S. and Hakala, J.: Multi-scheme chemical ionization inlet (MION) for fast
726 switching of reagent ion chemistry in atmospheric pressure chemical ionization mass spectrometry (CIMS)
727 applications, Atmos. Meas. Tech., doi:10.5194/amt-12-6635-2019, 2019.

728 Rothman, L. S., Gordon, I. E., Barber, R. J., Dothe, H., Gamache, R. R., Goldman, A., Perevalov, V. I., Tashkun, S.
729 A. and Tennyson, J.: HITEMP, the high-temperature molecular spectroscopic database, J. Quant. Spectrosc. Radiat.
730 Transf., doi:10.1016/j.jqsrt.2010.05.001, 2010.

731 Saiz-Lopez, A., Plane, J. M. C., Baker, A. R., Carpenter, L. J., Von Glasow, R., Gómez Martín, J. C., McFiggans, G.
732 and Saunders, R. W.: Atmospheric chemistry of iodine, Chem. Rev., doi:10.1021/cr200029u, 2012.

733 Sanchez, J., Tanner, D. J., Chen, D., Huey, L. G. and Ng, N. L.: A new technique for the direct detection of HO2
734 radicals using bromide chemical ionization mass spectrometry (Br-CIMS): Initial characterization, Atmos. Meas.
735 Tech., doi:10.5194/amt-9-3851-2016, 2016.

736 Schnitzhofer, R., Metzger, A., Breitenlechner, M., Jud, W., Heinritzi, M., De Menezes, L.-P., Duplissy, J., Guida,
737 R., Haider, S., Kirkby, J. and others: Characterisation of organic contaminants in the CLOUD chamber at CERN,
738 Atmos. Meas. Tech., 7(7), 2159–2168, 2014.

739 Schwehr, K. A., Santschi, P. H. and Elmore, D.: The dissolved organic iodine species of the isotopic ratio of
740 129I/127I: A novel tool for tracing terrestrial organic carbon in the estuarine surface waters of Galveston Bay,
741 Texas, Limnol. Oceanogr. Methods, doi:10.4319/lom.2005.3.326, 2005.

742 Sherwen, T., Evans, M. J., Carpenter, L. J., Andrews, S. J., Lidster, R. T., Dix, B., Koenig, T. K., Sinreich, R.,
743 Ortega, I., Volkamer, R., Saiz-Lopez, A., Prados-Roman, C., Mahajan, A. S. and Ordóñez, C.: Iodine's impact on
744 tropospheric oxidants: A global model study in GEOS-Chem, Atmos. Chem. Phys., doi:10.5194/acp-16-1161-2016,
745 2016.

746 Simpson, W. R., Brown, S. S., Saiz-Lopez, A., Thornton, J. A. and Von Glasow, R.: Tropospheric Halogen
747 Chemistry: Sources, Cycling, and Impacts, Chem. Rev., doi:10.1021/cr5006638, 2015.

748 Sipilä, M., Sarnela, N., Jokinen, T., Henschel, H., Junninen, H., Kontkanen, J., Richters, S., Kangasluoma, J.,
749 Franchin, A., Peräkylä, O., Rissanen, M. P., Ehn, M., Vehkamäki, H., Kurten, T., Berndt, T., Petäjä, T., Worsnop,
750 D., Ceburnis, D., Kerminen, V. M., Kulmala, M. and O'Dowd, C.: Molecular-scale evidence of aerosol particle
751 formation via sequential addition of HIO3, Nature, doi:10.1038/nature19314, 2016.

752 Spietz, P., Martín, J. G. and Burrows, J. P.: Effects of column density on i2 spectroscopy and a determination of i2
753 absorption cross section at 500 nm, Atmos. Chem. Phys., doi:10.5194/acp-6-2177-2006, 2006.

754 Spolaor, A., Gabrieli, J., Martma, T., Kohler, J., Björkman, M. B., Isaksson, E., Varin, C., Vallelonga, P., Plane, J.
755 M. C. and Barbante, C.: Sea ice dynamics influence halogen deposition to Svalbard, Cryosphere, doi:10.5194/tc-7-
756 1645-2013, 2013.

757 Stolzenburg, D., Simon, M., Ranjithkumar, A., Kürten, A., Lehtipalo, K., Gordon, H., Ehrhart, S., Finkenzeller, H.,
758 Pichelstorfer, L., Nieminen, T. and others: Enhanced growth rate of atmospheric particles from sulfuric acid, Atmos.
759 Chem. Phys., 20(12), 7359–7372, 2020.

760 Thalman, R. and Volkamer, R.: Temperature dependent absorption cross-sections of O2-O2 collision pairs between
761 340 and 630 nm and at atmospherically relevant pressure, Phys. Chem. Chem. Phys., doi:10.1039/c3cp50968k,
762 2013.

763 Tham, Y. J., Wang, Z., Li, Q., Yun, H., Wang, W., Wang, X., Xue, L., Lu, K., Ma, N., Bohn, B., Li, X., Kecorius,
764 S., Größ, J., Shao, M., Wiedensohler, A., Zhang, Y. and Wang, T.: Significant concentrations of nitryl chloride
765 sustained in the morning: Investigations of the causes and impacts on ozone production in a polluted region of
766 northern China, Atmos. Chem. Phys., doi:10.5194/acp-16-14959-2016, 2016.

767 Tham, Y. J., He, X.-C., Li, Q., Cuevas, C. A., Shen, J., Kalliokoski, J., Yan, C., Iyer, S., Lehmusjärvi, T., Jang, S.
768 and others: Direct field evidence of autocatalytic iodine release from atmospheric aerosol, Proc. Natl. Acad. Sci.,
769 118(4), 2021.

770 Vandaele, A. C., Hermans, C., Simon, P. C., Carleer, M., Colin, R., Fally, S., Mérienne, M. F., Jenouvrier, A. and
771 Coquart, B.: Measurements of the NO2 absorption cross-section from 42 000 cm-1 to 10 000 cm-1 (238-1000 nm) at
772 220 K and 294 K, J. Quant. Spectrosc. Radiat. Transf., doi:10.1016/S0022-4073(97)00168-4, 1998.

773 Vaughan, S., Gherman, T., Ruth, A. A. and Orphal, J.: Incoherent broad-band cavity-enhanced absorption
774 spectroscopy of the marine boundary layer species I2, IO and OIO, Phys. Chem. Chem. Phys.,
775 doi:10.1039/b802618a, 2008.

776 Wang, M., Kong, W., Marten, R., He, X. C., Chen, D., Pfeifer, J., Heitto, A., Kontkanen, J., Dada, L., Kürten, A.,
777 Yli-Juuti, T., Manninen, H. E., Amanatidis, S., Amorim, A., Baalbaki, R., Baccarini, A., Bell, D. M., Bertozzi, B.,
778 Bräkling, S., Brilke, S., Murillo, L. C., Chiu, R., Chu, B., De Menezes, L. P., Duplissy, J., Finkenzeller, H.,
779 Carracedo, L. G., Granzin, M., Guida, R., Hansel, A., Hofbauer, V., Krechmer, J., Lehtipalo, K., Lamkaddam, H.,
780 Lampimäki, M., Lee, C. P., Makhmutov, V., Marie, G., Mathot, S., Mauldin, R. L., Mentler, B., Müller, T., Onnela,
781 A., Partoll, E., Petäjä, T., Philippov, M., Pospisilova, V., Ranjithkumar, A., Rissanen, M., Rörup, B., Scholz, W.,
782 Shen, J., Simon, M., Sipilä, M., Steiner, G., Stolzenburg, D., Tham, Y. J., Tomé, A., Wagner, A. C., Wang, D. S.,
783 Wang, Y., Weber, S. K., Winkler, P. M., Wlasits, P. J., Wu, Y., Xiao, M., Ye, Q., Zauner-Wieczorek, M., Zhou, X.,
784 Volkamer, R., Riipinen, I., Dommen, J., Curtius, J., Baltensperger, U., Kulmala, M., Worsnop, D. R., Kirkby, J.,
785 Seinfeld, J. H., El-Haddad, I., Flagan, R. C. and Donahue, N. M.: Rapid growth of new atmospheric particles by
786 nitric acid and ammonia condensation, Nature, doi:10.1038/s41586-020-2270-4, 2020.

787 Washenfelder, R. A., Langford, A. O., Fuchs, H. and Brown, S. S.: Measurement of glyoxal using an incoherent
788 broadband cavity enhanced absorption spectrometer, Atmos. Chem. Phys., doi:10.5194/acp-8-7779-2008, 2008.

789

790

791 **Table 1: Cluster formation enthalpies of different species with bromide ions.** The cluster geometries are optimized
792 at the ωB97X-D/aug-cc-pVTZ-PP level at 298.15 K. The enthalpies are calculated at the DLPNO-CCSD(T)/def2-
793 QZVPP//ωB97xD/aug-cc-pVTZ-PP level at 298.15 K.

Cluster formation pathway	Formation enthalpies (kcal mol^{-1})
$Cl_2 + Br^- \rightarrow Cl_2 \cdot Br^-$	-22.3
$OIO + Br^- \rightarrow OIO \cdot Br^-$	-23.2
$IO + Br^- \rightarrow IO \cdot Br^-$	-24.5
$HIO_3 + Br^- \rightarrow HIO_3 \cdot Br^-$	-26.6
$HOI + Br^- \rightarrow HOI \cdot Br^-$	-26.9
$HIO_2 + Br^- \rightarrow HIO_2 \cdot Br^-$	-29.2
$I_2 + Br^- \rightarrow I_2 \cdot Br^-$	-33.7
$ICl + Br^- \rightarrow ICl \cdot Br^-$	-33.8
$IBr + Br^- \rightarrow IBr \cdot Br^-$	-36.7
$H_2SO_4 + Br^- \rightarrow H_2SO_4 \cdot Br^-$	-41.1
$I_2O_4 + Br^- \rightarrow I_2O_4 \cdot Br^-$	-42.6
$I_2O_5 + Br^- \rightarrow I_2O_5 \cdot Br^-$	-53.2

794

795 **Table 2: Fragmentation reaction enthalpies of different species with bromide ions.** The cluster geometries are
796 optimized at the ωB97X-D/aug-cc-pVTZ-PP level at 298.15 K. The enthalpies are calculated at the DLPNO-
797 CCSD(T)/def2-QZVPP//ωB97xD/aug-cc-pVTZ-PP level at 298.15 K.

Cluster fragmentation pathway	Fragmentation enthalpies (kcal mol^{-1})
$Cl_2 \cdot Br^- \rightarrow Cl_2 + Br^-$	22.3
$Cl_2 \cdot Br^- \rightarrow BrCl + Cl^-$	22.3
$HIO_3 \cdot Br^- \rightarrow HIO_3 + Br^-$	26.6
$HIO_3 \cdot Br^- \rightarrow IO_3^- + HBr$	20.8
$HIO_3 \cdot Br^- \rightarrow IO_2^- + HOBr$	52.0
$HOI \cdot Br^- \rightarrow HOI + Br^-$	26.9
$HOI \cdot Br^- \rightarrow IO^- + HBr$	57.7
$HOI \cdot Br^- \rightarrow I^- + HOBr$	31.3
$HIO_2 \cdot Br^- \rightarrow HIO_2 + Br^-$	29.2
$HIO_2 \cdot Br^- \rightarrow IO_2^- + HBr$	43.8
$HIO_2 \cdot Br^- \rightarrow IO^- + HOBr$	42.2
$I_2 \cdot Br^- \rightarrow I_2 + Br^-$	33.7

$I_2 \cdot Br^- \rightarrow IBr + I^-$	33.8
$ICl \cdot Br^- \rightarrow ICl + Br^-$	33.8
$ICl \cdot Br^- \rightarrow IBr + Cl^-$	39.8
$ICl \cdot Br^- \rightarrow BrCl + I^-$	42.0
$IBr \cdot Br^- \rightarrow IBr + Br^-$	36.7
$IBr \cdot Br^- \rightarrow Br_2 + I^-$	39.4
$H_2SO_4 \cdot Br^- \rightarrow H_2SO_4 + Br^-$	41.1
$H_2SO_4 \cdot Br^- \rightarrow HSO_4^- + HBr$	27.9

798

799 **Table 3: Calibration coefficients for selected species.**

Species	Calibration coefficient (molec cm^{-3} cps cps^{-1})	Detection limit (molec cm^{-3})
[a] I_2	2.7×10^{10}	3.8×10^5
[a] H_2SO_4	4.1×10^{10}	2.0×10^5
[b] I_2	6.3×10^{10}	8.8×10^5
[b] Cl_2	3.5×10^{11}	n/a
[b] HOI	3.3×10^{11}	5.8×10^6
[c] HIO_3	4.1×10^{10}	1.2×10^5

800 [a] Inter-method calibrations

801 [b] Offline calibrations

802 [c] Derived from dissociation enthalpies